

Dynamics and mixing of a sonic jet in a supersonic turbulent crossflow

By S. Kawai AND S. K. Lele

1. Motivation and objective

Inside a supersonic combustor, due to the limited flow residence time, the enhancement of mixing of jet fuel and crossflow air is a critical issue in developing supersonic engines. Understanding the physical mechanisms of the turbulent jet mixing in supersonic flows remains a significant challenge in both experimental and numerical investigations.

Several experimental investigations have been conducted to understand the mechanisms of the jet mixing in a supersonic crossflow, which include detailed velocity measurements (Santiago & Dutton 1997), time-averaged wall pressure measurements (Everett *et al.* 1998), and temporally resolved flow visualizations and mixing characteristics with non-reactive (Gruber *et al.* 1995; VanLerberghe *et al.* 2000) and combustible gaseous jets (Ben-Yakar *et al.* 2006; Heltsley 2009). These measurements show the overall flow features and the dynamics of the jet shear layer, shocks, and ignitions. However, because of the difficulty in measuring the high-speed complex unsteady flowfields, experimental data are mainly obtained for certain two-dimensional slices of the flowfield.

To obtain additional insights into the three-dimensional unsteady flow occurring in a jet in a supersonic crossflow (JISC), large-eddy simulation (LES) (von Lavante *et al.* 2001) and detached-eddy simulation (Peterson *et al.* 2006) have been performed and have shown the presence of some large-scale structures. However, these large-scale structures are somewhat obscure, and fine turbulent eddy structures are missing in these simulations. This is primarily because the conventional low-order upwind-biased finite volume schemes were employed to discretize the governing equations with limited grid resolution in these calculations. These schemes work well for discontinuity capturing but are too dissipative for use in LES to properly resolve the broadband scales of turbulence. It is essential for LES to properly resolve the energy-containing scales of turbulence and avoid damping the turbulence artificially. Therefore, LES of the supersonic jet mixing presents challenges for simultaneously capturing complex unsteady shocks and contact surfaces and resolving the broadband turbulent eddying motions present in high Reynolds number flows.

The objective of this brief is to understand the key physics of the jet mixing in a supersonic crossflow underlying the observed unsteady phenomena. Emphasis is placed on identifying the key vortex structures and large-scale dynamics in the flow that are responsible for the jet mixing. LES of an under-expanded sonic jet injection into a supersonic turbulent crossflow reported in the experiment of Santiago & Dutton (1997) is performed to elucidate the physics of the jet mixing. In order to properly resolve the turbulence while capturing the discontinuities, we use a high-order non-dissipative compact differencing scheme (Lele 1992) coupled with a recently developed localized artificial diffusivity (LAD) methodology (Kawai *et al.* 2009). We finally note that the results presented in this brief are obtained from new improved calculations compared to the results reported in last year (Kawai & Lele 2008a) in terms of the improvement of LAD method and a supersonic turbulent crossflow conditions with a highly resolved mesh.

2. Mathematical models

The spatially filtered compressible Navier-Stokes equations for an ideal non-reactive gas are solved in a strong conservative form. In addition to the Navier-Stokes equations, the transport equation for a passive scalar of jet fluid (Y) is solved to investigate the mixing between the jet and crossflow fluids. The compressible LES equations include additional subgrid-scale stress, heat flux, and species diffusion terms that need to be modeled.

2.1. Numerical schemes

The governing equations are solved in generalized curvilinear coordinates, where spatial derivatives are evaluated by a sixth-order compact differencing scheme (Lele 1992).

The localized artificial diffusivity (LAD) method (Kawai *et al.* 2009) is used to capture the discontinuities in the flow. The method is based on adding grid-dependent artificial fluid transport coefficients to the physical transport coefficients as proposed by Cook (2007),

$$\mu = \mu_f + \mu^*, \quad \beta = \beta_f + \beta^*, \quad \kappa = \kappa_f + \kappa^*, \quad D = D_f + D^*, \quad (2.1)$$

where μ is the dynamic (shear) viscosity, β is the bulk viscosity, κ is the thermal conductivity, and D is the diffusion coefficient for the passive scalar. The f subscripts and asterisks denote fluid and artificial transport coefficients. According to Cook (2007) the artificial fluid properties μ^* , β^* , κ^* , and D^* serve as a multi-purpose model for the subgrid-scale transport, for shock-capturing, contact surface capturing, and material interface capturing. μ_f is computed by Sutherland's law, and $\beta_f = 0$. κ_f is computed by $\kappa_f = \frac{\mu_f C_p}{Pr}$ where C_p is the specific heat constant and Pr ($=0.72$) is Prandtl number. D_f is computed by $D_f = \frac{\mu_f}{\rho Sc}$ where Sc is Schmidt number and is on the order of unity.

The localized artificial diffusivity on a multi-dimensional generalized coordinate system is modeled based on (Cook 2007; Kawai & Lele 2008b; Mani *et al.* 2009; Kawai *et al.* 2009) as:

$$\mu^* = C_\mu \rho \overline{\left| \sum_{l=1}^3 \frac{\partial^4 S}{\partial \xi_l^4} \Delta \xi_l^4 \Delta_{l,\mu}^2 \right|}, \quad (2.2)$$

$$\beta^* = C_\beta \rho f_{sw} \overline{\left| \sum_{l=1}^3 \frac{\partial^4 \nabla \cdot \mathbf{u}}{\partial \xi_l^4} \Delta \xi_l^4 \Delta_{l,\beta}^2 \right|}, \quad f_{sw} = \frac{H(-\nabla \cdot \mathbf{u})(\nabla \cdot \mathbf{u})^2}{(\nabla \cdot \mathbf{u})^2 + (\nabla \times \mathbf{u})^2 + \varepsilon} \quad (2.3)$$

$$\kappa^* = C_\kappa \frac{\rho c_s}{T} \overline{\left| \sum_{l=1}^3 \frac{\partial^4 e}{\partial \xi_l^4} \Delta \xi_l^4 \Delta_{l,\kappa} \right|}, \quad (2.4)$$

$$D^* = C_D c_s \overline{\left| \sum_{l=1}^3 \frac{\partial^4 Y}{\partial \xi_l^4} \Delta \xi_l^4 \Delta_{l,D} \right|} + C_Y c_s \overline{[Y-1]H(Y-1) - Y[1-H(Y)]\Delta_Y}, \quad (2.5)$$

where C_μ , C_β , C_κ , C_D , and C_Y are dimensionless user-specified constants: ρ is the density, S is the magnitude of the strain rate tensor, \mathbf{u} is the velocity vector, e is the internal energy, c_s is the speed of sound, T is the temperature, and H is the Heaviside function. The more detailed definition of the notation and analysis of the performance of the present LAD method for LES of compressible turbulent flows may be found in Kawai *et al.* (2009).

The dimensionless user-specified constants in Eqs. 2.2–2.5 are set to $C_\mu=0.002$, $C_\beta=1.75$,

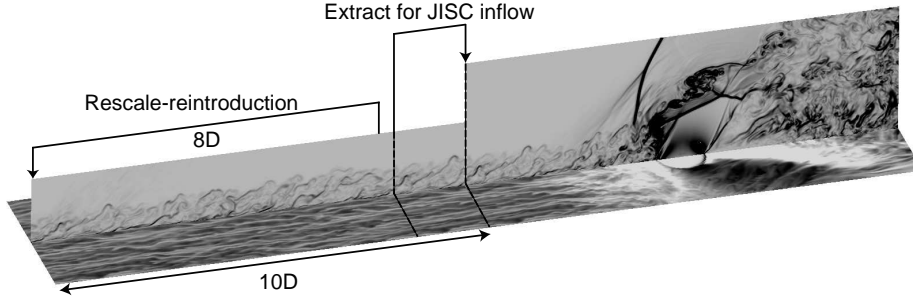


FIGURE 1. JISC with incoming supersonic turbulent boundary layer. Density gradient magnitude contours at midline plane $z/D=0$ and streamwise velocity contours at wall-parallel plane close to the wall ($y^+ = 18.5$).

$C_\kappa=0.01$, $C_D=0.01$, and $C_Y=100$ in this study based on our previous investigations (Kawai & Lele 2008b; Kawai *et al.* 2009). A van Driest wall damping function multiplies the grid spacing ($\Delta_{l,\mu}$ and $\Delta_{l,\beta}$) in the present LAD method to force the artificial viscosity to vanish in the near wall portion of the boundary layers.

An eighth-order low-pass spatial filtering scheme (Lele 1992; Gaitonde & Visbal 2000), with $\alpha_f = 0.495$, is applied to the conservative variables once in each direction after every three time-steps in order to ensure numerical stability. The fully implicit ADI-SGS scheme (Iizuka 2006) is used for time integration. The implicit portion of the algorithm uses second-order accurate three-point backward differencing for the derivative. Three steps of sub-iterations are adopted to minimize the errors owing to the linearization in the implicit scheme. In the present study, the non-dimensional computational time step is fixed to $\Delta t U_\infty / D = 9.6 \times 10^{-4}$ at which the maximum inviscid Courant-Friedrichs-Lewy (CFL) number is less than 1.0, where U_∞ is the crossflow velocity, and D is the diameter of the nozzle exit. The present time-integration scheme with the time-step size should be sufficiently accurate based on our previous study (Kawai *et al.* 2009).

2.2. Flow conditions

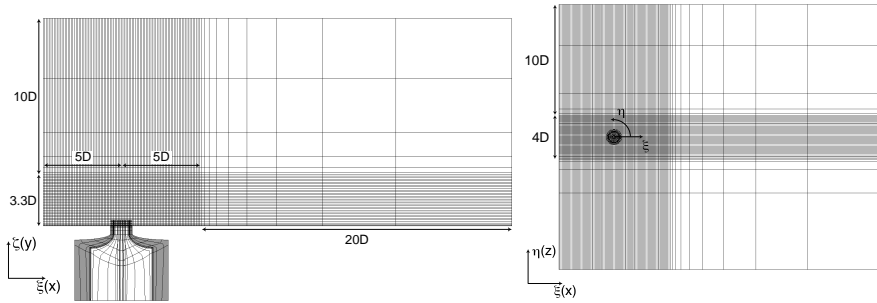
The flow condition examined in this study is based on the experiments of Santiago & Dutton (1997), Everett *et al.* (1998), and VanLerberghe *et al.* (2000). The computation uses a freestream Mach number of $M_\infty=1.6$ and a Reynolds number based on the freestream conditions and the diameter of the nozzle exit $Re_D = \frac{\rho_\infty U_\infty D}{\mu_\infty} = 2.4 \times 10^4$. The density and pressure ratio between the nozzle chamber and crossflow are $\rho_{0j}/\rho_\infty = 5.55$ and $p_{0j}/p_\infty = 8.40$. Based on these flow conditions, the resulting jet-to-crossflow momentum flux ratio is $J = \rho_j u_j^2 / \rho_\infty u_\infty^2 = 1.7$, where the j subscript indicates properties at the nozzle exit. Following the experiments, we use the same fluid, i.e., air, for both the jet and crossflow fluids. However in order to maintain the LES resolution requirement under currently acceptable computational costs, a Reynolds number approximately six times lower than the Re_D in the experiments is used in the simulation. Although the Reynolds number differs, the upstream boundary layer thickness is matched with the experiment at $x/D = -5$ where $\delta_{99} = 0.775D$ (3.1 mm).

2.3. Inflow condition for crossflow turbulence

Figure 1 shows the schematic of the LES of JISC. We conduct the concurrent simulation of a supersonic turbulent boundary layer (STBL) shown in the left half in Fig. 1 that is coupled with the JISC computation in the right half. The inflow conditions for the

Grid	N_ξ	N_η	N_ζ	Total (million)	Δx^+	Δy^+	Δz^+
JISC background mesh	551	243	204	27.3	14.5	1–14.5	14.5
STBL mesh	361	243	120	10.5	20.5	1–14.5	14.5

TABLE 1. Computational grids for JISC background mesh and STBL mesh.

FIGURE 2. Computational grids (every fifth grid point). Side view at symmetric plane $z/D=0$ on left and top view on right.

JISC are extracted from the plane of the concurrent STBL at the location where $\delta_{99} = 0.775D$ (3.1 mm). In the concurrent LES of STBL, the Reynolds number is matched with the JISC simulation, $Re_D = 2.4 \times 10^4$. The corresponding Reynolds number based on the boundary layer thickness at the extracted plane for the JISC simulation is $Re_{\delta_{99}} = 18600$. The rescaling-reintroducing method (Urbin & Knight 2001) is used to generate the inflow conditions for the STBL as shown in Fig. 1. The flow quantities at the $8D$ downstream location are rescaled and reintroduced as inflow conditions for the LES of STBL. We note that the experimental measurement of the mean velocity profile of the approaching boundary layer shows a turbulent boundary layer profile (Santiago & Dutton 1997).

2.4. Computational grids

Figure 2 shows the grid geometry of the computational domain for the JISC simulation employed in the present study. Every fifth grid point is represented in the figure. The overset grids consist of three structured grids: background, nozzle, and nozzle-axis grids. The nozzle-axis grid covers the singular line in the nozzle grid. The geometry of the nozzle matches the experiment (Santiago & Dutton 1997; Everett *et al.* 1998; VanLerberghe *et al.* 2000). A uniformly spaced grid is adopted in streamwise and spanwise directions within the computational test section, $-5 \leq x/D \leq 5$ and $-2 \leq z/D \leq 2$ where the center of the nozzle exit is $x/D = y/D = 0$. In the wall-normal direction, the grid is clustered near the wall in the region $y/D=0$ to 0.3 and then a uniformly spaced grid is used for $y/D=0.3$ to 3.3 . Table 1 summarizes the number of grid points and the grid resolution. The grid resolutions for the nozzle and nozzle-axis meshes are designed based on the background mesh. The total number of grid points is 38.5 million points.

Although not shown in this brief, we conducted a series of progressive mesh refinement and validation against available experimental data. The statistics obtained by the present LES show good agreement with the experiments, and the mesh refinement shows reasonable grid convergence in the predicted mean and turbulent flow quantities (Kawai

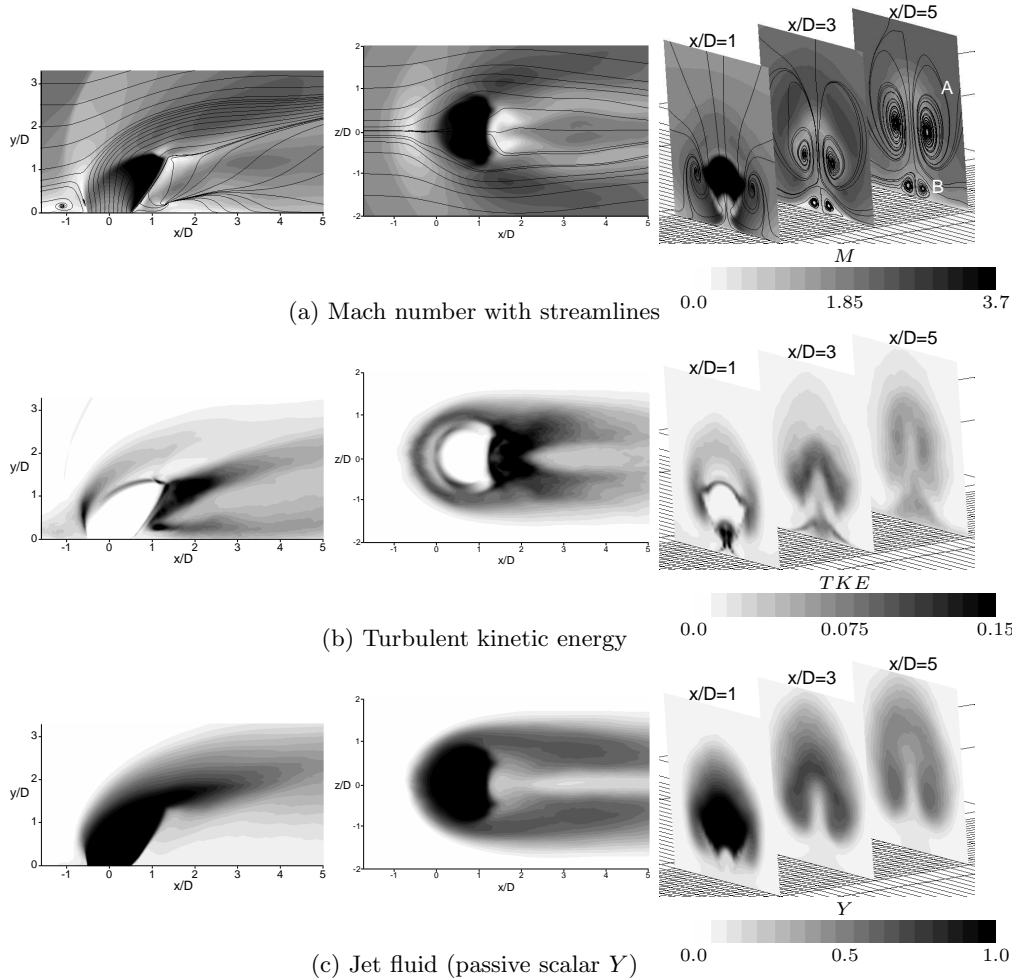


FIGURE 3. Time-averaged Mach number distributions with streamlines, time-averaged turbulent kinetic energy, and jet fluid (passive scalar Y) distributions: side view at midline plane $z/D=0$ on the left, top view at wall-parallel plane $y/D=1$ in the middle, and cross-view planes of $x/D=1$, 3 and 5 on the right. Twenty equally spaced contours are shown.

& Lele 2009). The progressive mesh refinement in combination with the high-resolution non-dissipative numerical scheme allows for proper resolution of the turbulence. Therefore the current LES is suited for exploration of the dynamics and mixing of the jet in a supersonic turbulent crossflow.

3. Time-averaged flowfields

Figure 3 (a) shows time-averaged Mach number distributions with streamlines at midline, wall-normal, and cross-view planes. The Mach number contours clearly show the shock structure, such as the front bow shock, barrel shock, Mach disk, reflected shock from the triple line (the intersection of the barrel shock and Mach disk), and separation shock at the front of bow shock. The upstream separation shock is not as strong as the other shocks, the contours slightly change from the dark gray to light gray (from

pre-shock to post-shock) and interact with the bow shock. The streamlines show that most of the jet fluid passes through the barrel shock and Mach disk and then turns downstream. Upstream of the jet, a recirculation region is observed. The recirculation forms a horseshoe separation vortex ahead of the foot of the bow shock. The horseshoe vortex curves sideways from the midline plane $z/D=0$. The top view shows that the streamlines diverge laterally after the crossflow deflects through the bow shock and then converge downstream owing to the low pressure behind the jet. Two pairs of counter-rotating vortices are clearly visible downstream of the jet injection in the cross view; one is the counter-rotating jet vortices [A in Fig. 3 (a)] as often discussed in the literature (Gruber *et al.* 1995; Santiago & Dutton 1997; Viti *et al.* 2009), and the other is the pair of boundary layer separation vortices [B in Fig. 3 (a)] along the symmetric plane induced by the suction of the counter-rotating jet vortices.

Time-averaged turbulent kinetic energy (TKE), $(\langle u'u' \rangle + \langle v'v' \rangle + \langle w'w' \rangle)/2U_\infty^2$, and jet fluid (passive scalar Y) distributions are shown in Fig. 3 (b) and (c). Three high TKE regions are identified at the windward and leeward boundaries of the jet and under the leeward jet boundary in the side view. The first two high TKE regions surround the jet boundary. As shown in the cross view in Fig. 3 (b), the high TKE under the leeward jet boundary observed in the side view originates from the boundary layer separation under the counter-rotating jet vortices along the symmetric plane. These high-intensity regions in the TKE correspond to the regions where strong vortex structures are observed in the instantaneous flowfield, as will be discussed in Section 4. Time-averaged jet fluid distributions in Fig. 3 (c) show that the jet fluid is progressively diluted in the regions where high TKE is observed, suggesting that the turbulent eddies are responsible for the turbulent stirring and subsequent mixing. The cross view shows the jet fluid entrainment into the boundary layer separation vortices downstream of the jet.

4. Instantaneous flowfields

4.1. Two-dimensional slices of flowfields

Fig. 4 shows instantaneous snapshots of density gradient magnitude and passive scalar of jet fluid. Side-, top-, and cross-view planes are obtained at $z/D=0$, $y/D=1$, and $x/D=1, 3$ and 5 . The high-order compact differencing scheme with localized artificial diffusivity methodology captures the three-dimensional unsteady front bow shock, upstream separation shock, barrel shock, Mach disk, acoustic waves, and contact surfaces without spurious wiggles and also simultaneously resolves a broad range of scales of turbulence. The turbulent eddies in the incoming boundary layer interact with the front bow shock and the windward jet.

Most of the jet fluid passes through the barrel shock and Mach disk; jet mixing progressively occurs after the jet fluid passes through the shocks. The vortex structures in the windward and leeward jet boundaries break down to finer well-developed turbulent eddy structures downstream. The turbulent structures play an important role in determining the behavior of jet fluid stirring and subsequent mixing as clearly shown in the snapshots of the passive scalar. Because the jet fluid that passes through the barrel shock has larger velocity than the crossflow that passes through the bow shock, vortices developed along the windward jet boundary roll counter-clockwise, as observed in the side view. The vortices also roll in the spanwise direction along the windward jet boundary, as observed in the top view. Therefore, these vortices do not form a clear vortex ring but form complex three-dimensional vortex ring-like structures as will be discussed below. In

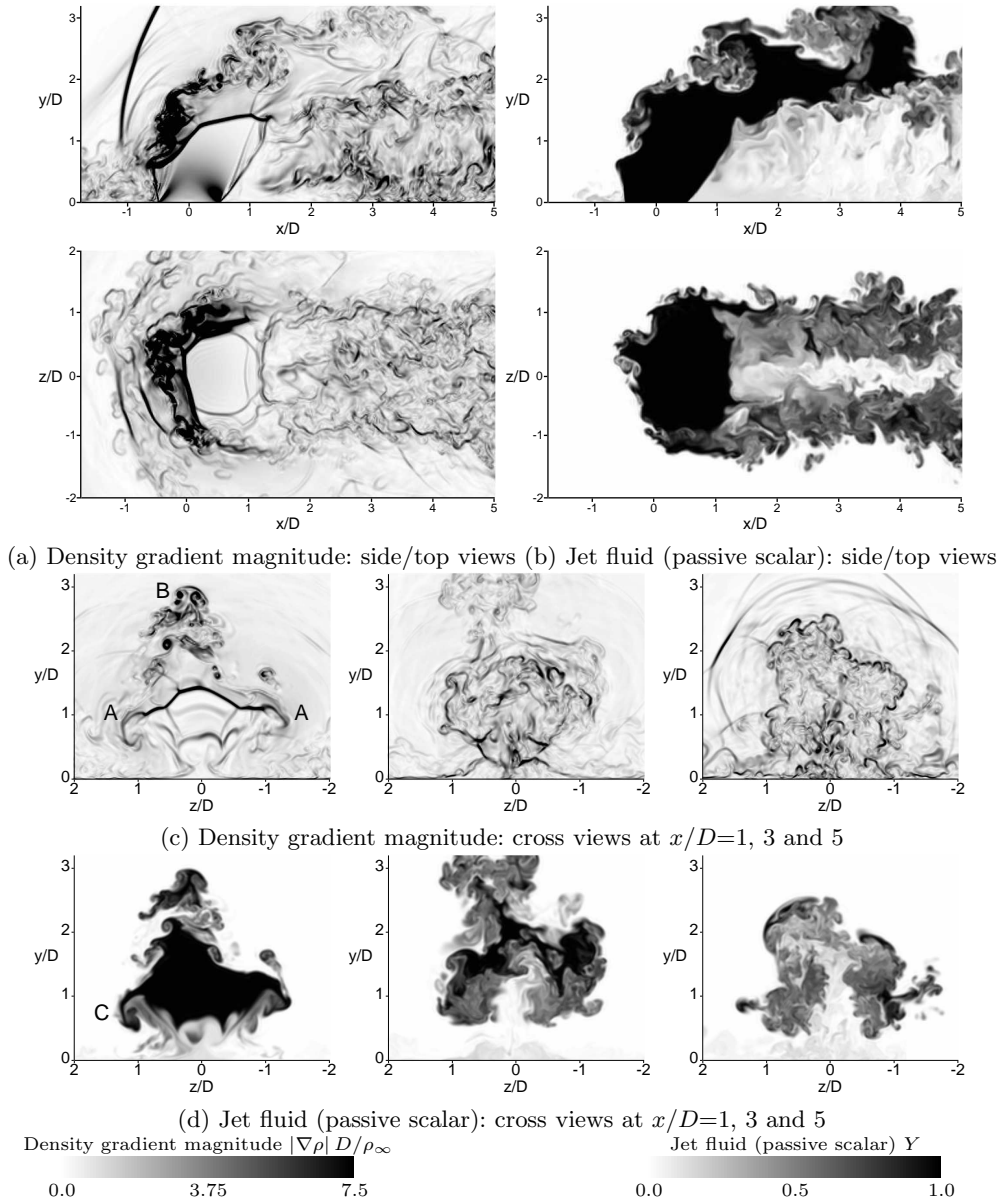


FIGURE 4. Instantaneous snapshots of density gradient magnitude and passive scalar of jet fluid at midline plane $z/D=0$ (top), wall-parallel plane $y/D=1$ (middle), and cross-view planes $x/D=1, 3$ and 5 (bottom two, from left to right).

addition to these vortices, additional vortex structures are observed under the leeward jet boundary in the side view. These vortices originate in the boundary layer separation vortices and the vortices along the pair of the counter-rotating jet vortices (spanwise stirring) as shown in the cross views. The boundary layer separation vortices exist along the symmetric plane downstream of the jet induced by the suction of the counter-rotating

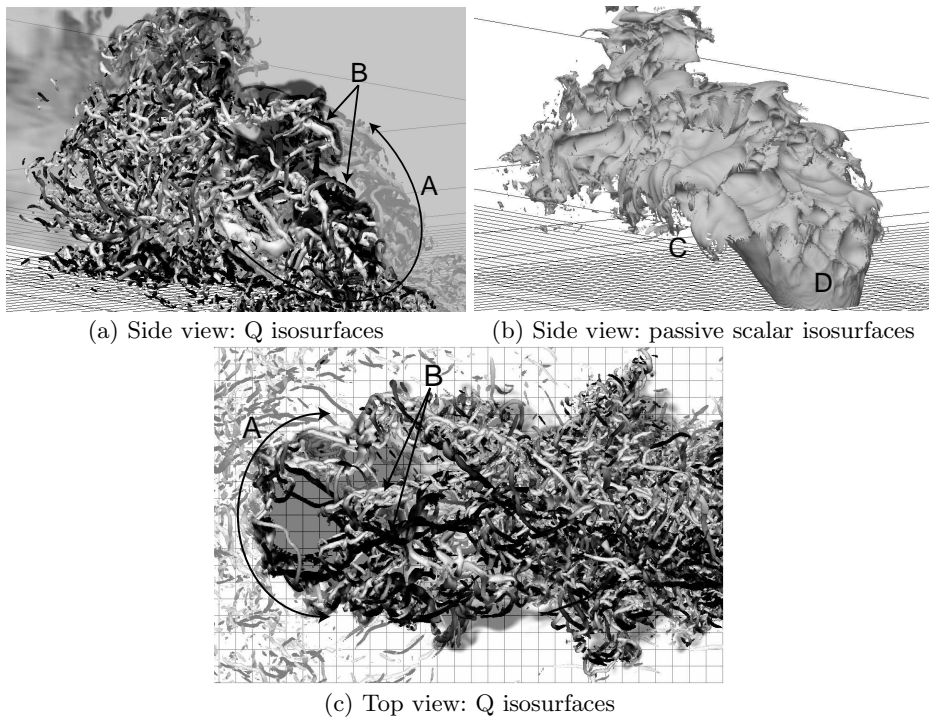


FIGURE 5. Instantaneous snapshots of vortex structures in side and top views and jet structures in side view. (a) and (c): isosurfaces of the second invariant of velocity gradient tensor Q colored by streamwise vorticity. Passive scalar of jet fluid distributions in transparent gray colored contour surface at the midline plane $z/D=0$ in the side view and wall-parallel plane $y/D=1$ in the top view. (b): isosurfaces of $Y=0.95$ passive scalar of jet fluid.

jet vortices. These turbulent structures create the high TKE regions as observed around the jet boundary and under the leeward jet boundary in Fig. 3 (b).

On the leeward side of the jet, the side view of the jet fluid [Fig. 4 (b)] shows thin filaments of jet fluid that are aligned normal to the jet trajectory. These filaments are observed close to the symmetry plane where the pair of counter-rotating jet vortices induces upwash, the boundary layer separates, and the boundary layer fluid is scooped up and entrained into the jet vortices. Su & Mungal (2004) observe similar thin scalar filaments in their low-speed jet in crossflow experiments. They suggest that these filaments probably correspond to the wake vortices discussed by Fric & Roshko (1994). Fig. 4 (d) shows the jet fluid entrainment into the boundary layer separation bubble along the symmetric plane downstream of the jet.

4.2. Three-dimensional vortex and jet structures

The three-dimensional features of vortex structures in its side and top views are visualized by the instantaneous isosurfaces of the second invariant of velocity gradient tensor Q in Fig. 5 (a) and (c). The Q isosurfaces are colored by streamwise vorticity, which mean that dark and light surfaces show clockwise and counter-clockwise rotating vortices respectively with the axis in the streamwise direction. The transparent gray colored contour surface is the passive scalar of jet fluid distributions at the midline plane $z/D=0$ in the side view and the wall-parallel plane $y/D=1$ in the top view. Isosurfaces at $Y=0.95$ of the jet fluid are shown in Fig. 5 (b) to visualize the three-dimensional feature of the jet

structures. Relatively fine vortex structures upstream of the jet injection show unsteady vortical motion inside the upstream recirculation region, which forms a horseshoe vortex in the time-averaged flowfields.

Clockwise and counter-clockwise rotating strong longitudinal vortices are clearly observed by dark- and light-colored surfaces in the top view. The dark-colored clockwise rotating longitudinal vortices are observed mainly in the lower half of the top view and the counter-clockwise vortices are in the upper half. These longitudinal vortices form two groups of counter-rotating vortices as shown in Fig. 5 (a) and (c). One group is a U-shaped pair of counter-rotating vortices that develop sideways from the symmetry plane with an upward inclination as shown by A in Fig. 5 (a) and (c) [also in Fig. 4 (c) and (d) at $x/D=1$ plane], which forms the pair of counter-rotating jet vortices in the mean flowfield as shown in the cross view of Fig. 3 (a). The other group is the pair of counter-rotating vortices above the U-shaped vortices observed around the symmetry plane [B in Fig. 5 (a) and (c), and also in Fig. 4 (c) and (d) at $x/D=1$ plane], which is called upper trailing vortex in Viti *et al.* (2009).

Along the longitudinal vortices, relatively small-scale hairpin-like vortices (gray-colored vortices) that do not have a vortex axis in the streamwise direction are generated further downstream. The relatively large-scale longitudinal vortex structures break down to finer and more random well-developed turbulent structures downstream approximately at $x/D=2-3$. The isolated regions of vortex structures and resultant high *TKE* observed under the leeward jet boundary in the side view [Figs. 4 and 3 (b)] are due to these fine vortex structures along the jet boundary and the boundary layer separation vortices along the symmetric plane induced by the suction of the U-shaped jet vortices.

Looking at the instantaneous jet structures shown in Fig. 5 (b), the jet surface is elongated along the relatively large-scale U-shaped longitudinal vortex structures [an example is observed at location C, also visible in Fig. 4 (d) at $x/D=1$ plane]. In the developed turbulent region, the jet surface also breaks down to finer and more random structures, indicating the importance of these eddy structures that determine the behavior of jet fluid stirring and subsequent mixing. Interestingly, the windward jet surface at the location D shows fish-scale-like structures. The structures are more complex than roller structures associated with quasi-ring like vortices. This complex pattern is perhaps an effect of the impinging turbulent boundary layer structures.

4.3. Large-scale dynamics of shocks and jet

The simulated unsteady flowfield shows noticeable large-scale dynamics in the deformation of shock structures and associated vortex formation that entrains the crossflow and enhances the subsequent windward jet mixing. Time-series pressure data inside the upstream recirculation region and representative time-series snapshots of the passive scalar of jet fluid overlapped with negative dilatation contours at midline plane are shown in Fig. 6 to illustrate these related dynamics. The negative dilatation contours highlight the compression in the flow such as shock structures and acoustic waves. The pressure history data is obtained at location A in snapshot Fig. 6 (a). These twelve snapshots (a)–(l) are taken at the time corresponding to the markers in the pressure history. The simulated unsteady flowfield illustrates that the pressure fluctuation inside the recirculation region upstream of the jet is coupled with the large-scale dynamics of the deforming barrel shock and bow shock and the accompanied large-scale vortex formation from the windward jet boundary. During the large-scale dynamics the barrel shock shows a kink in the time-series images.

Corresponding to the pressure rise from time Fig. 6 (a) to (d) in the pressure history,

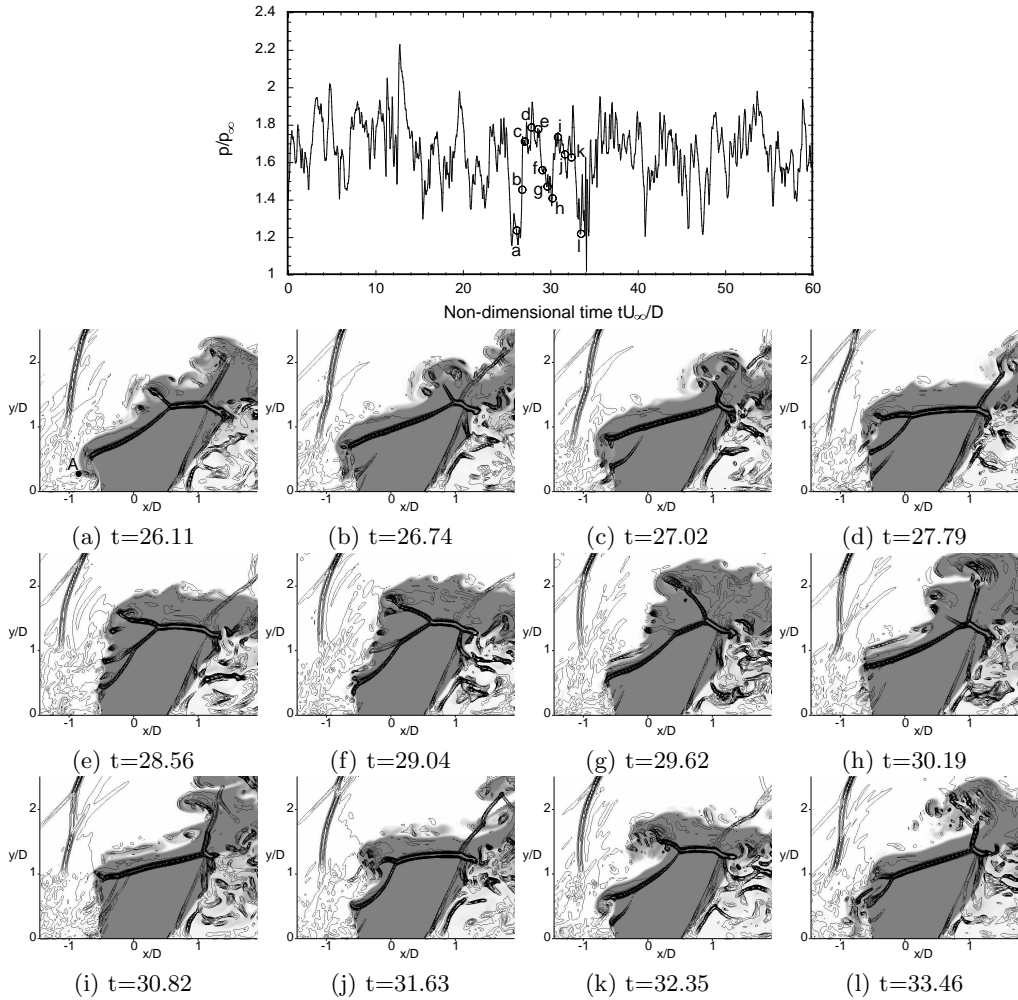


FIGURE 6. Time-series pressure data inside the upstream recirculation region and representative time-series snapshots of jet fluid (passive scalar Y) overlapped with negative dilatation contours at midline plane $z/D=0$. Non-dimensional time, $t = t^* \times U_{\infty}^*/D^*$.

the degree of expansion at the windward side of the nozzle edge reduces in order to keep the pressure balance across the jet boundary. Because of the less expansion (lower Mach number distribution along the jet boundary) at time (b) to (d), the jet shear layer is able to support the rapid growth of instability waves and starts to fluctuate. By way of contrast the jet shear at time (a) does not show such fluctuations.

Once the jet shear layer starts to fluctuate, a local shock wave appears within the jet because of the blockage of the supersonic jet by the deflected shear layer. Then, the local shock grows and connects to the original barrel shock, creating a kink in the barrel shock as shown in snapshot (d). In this time window, a second local shock wave appears and connects to the first local shock wave, showing the double kink in the barrel shock at time (e). The double kink in the barrel shock is not always present, and the following time window shows a single kink in the barrel shock as shown in snapshot (j). Once the kink appears, it moves downstream with an accompanying large-scale vortex, and

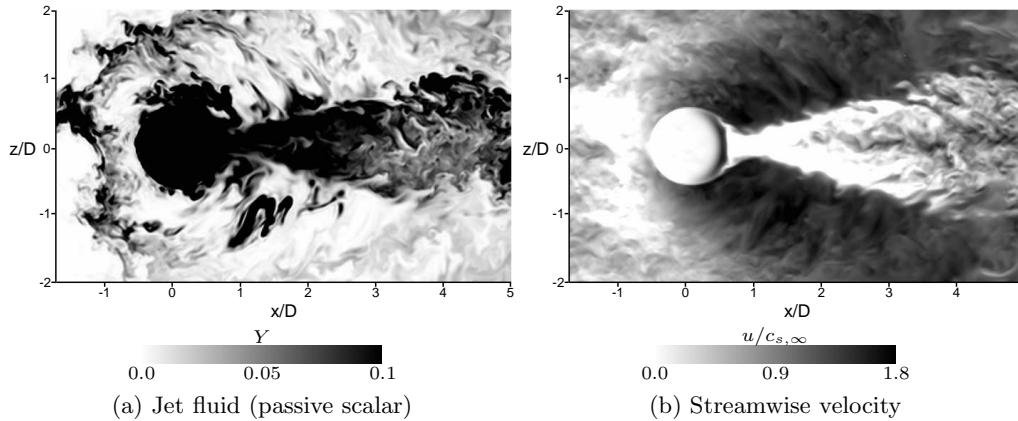


FIGURE 7. Jet fluid entrainments in upstream and downstream boundary layer separation bubbles. Instantaneous snapshots of passive scalar of jet fluid and streamwise velocity at wall-parallel plane close to the wall $y/D=0.1$.

the jet shear layer rapidly deflects along the shock. The three shocks interact at the kink, creating a triple point. The large-scale vortex entrains the crossflow, which stirs the jet fluid and enhances subsequent jet mixing. During the large-scale dynamics, an acoustic wave is generated and propagates upstream; it interacts with the bow shock [an example is observed in snapshots (h) and (i)]. This interaction causes large-scale unsteady oscillation of the bow shock. Similar dynamics occur following this large-scale dynamics as shown in snapshot (i)–(l).

Although the processes of the large-scale dynamics are discussed with reference to a certain time window, these dynamics are repeated numerous times during the LES time history. The frequency (Strouhal number) of the dynamics is found $St = fD/U_\infty = 0.4 \sim 0.6$. Similar large-scale dynamics of the barrel shock, bow shock, and accompanied large-scale vortex are also observed in the experiment (VanLerberghe *et al.* 2000). Ben-Yakar *et al.* (2006) also show similar front bow shock deformation and vortex formation in their consecutive Schlieren images, although the flow conditions are different from the present LES.

Interestingly, once large-scale counter-clockwise roll-up of the windward jet shear layer occurs immediately after the jet passing through the barrel shock, the jet fluid is entrained into a region upstream of the jet as shown in snapshots (a)–(c) and (k)–(l). The upstream entrainment of the jet fluid is also repeated in time associated with the large-scale dynamics of the shock waves and jet. Fig. 7 further illustrates the repeated upstream jet mixing, also the jet fluid entrainment into the boundary layer separation bubble along the symmetric plane downstream of the jet as discussed in Fig. 4 (d). Instantaneous snapshot of the jet fluid and streamwise velocity at a wall-parallel plane close to the wall ($y/D=0.1$) obtained by the LES is shown. Note that the passive scalar of jet fluid ranges from 0.0 to 0.1 in the figure. The plane intersects the instantaneous upstream and downstream separation regions [light colored regions in Fig. 7 (b)] that form the horseshoe vortex and a pair of counter-rotating boundary layer separation vortices along the symmetric plane, respectively, in the mean flow. The jet fluid entrainment is clearly observed along the upstream and downstream boundary layer separation bubbles. The upstream jet fluid entrainment occurs intermittently associated with the repeated large-scale dynamics, although the jet mixing in the downstream separation bubble is

continuous. These jet fluid entrainments may support the ignition of injected fuel along the separation regions upstream and downstream of the jet injection close to the wall for a reactive species. Experimental OH-PLIF measurements by Ben-Yakar *et al.* (2006) and Heltsley (2009) show a strong OH-PLIF signal along these separation regions although the flow conditions are different from the present LES. This indicates that the jet fluid mixing and resultant ignition occur along these upstream and downstream separation regions. The experimental result supports the mechanism of the jet fluid entrainment along the separation bubbles observed in the present LES.

5. Conclusions and future work

Large-eddy simulation (LES) of an under-expanded sonic jet injection into a supersonic turbulent crossflow was conducted to obtain insights into the key physics of the jet mixing underlying the observed unsteady phenomena.

Key physics of the jet mixing in a supersonic crossflow have been highlighted. Relatively large-scale clockwise and counter-clockwise rotating longitudinal vortices form two pairs of counter-rotating vortices. Relatively small-scale hairpin-like vortices are generated along the longitudinal vortices. The relatively large-scale longitudinal vortex structures break down to finer and random well-developed turbulent structures in the downstream of the hairpin vortices. The jet surfaces are elongated along the relatively large-scale longitudinal vortex structures and break down to finer and more random structures in the developed turbulent region, indicating the importance of these eddy structures that determine the behavior of jet fluid stirring and subsequent mixing.

The simulated unsteady flowfield shows noticeable repeated large-scale dynamics of the deformation of shock structures and accompanying vortex formation. Pressure fluctuations inside the recirculation region are coupled with the large-scale unsteady dynamics of the barrel shock and the bow shock deformation and accompanied large-scale vortex formation in the windward jet boundary. During the repeated large-scale dynamics, rolled-up windward jet shear layer is entrained into an upstream separation region, showing the intermittent upstream jet fluid mixing. The simulated flowfield also shows the continuous jet fluid entrainment into the boundary layer separation bubble downstream of the jet injection.

Future work will focus on analyzing the LES data in more depth. Further analysis of the physical mechanisms of the jet mixing and the repeated large-scale dynamics in shock waves and jet fluid will be pursued.

Acknowledgements

This work is supported by Air Force Office of Scientific Research (AFOSR) Multidisciplinary University Research Initiative (MURI) Program (Grant FA9550-04-1-0387). Computer time was provided by JAXA Supercomputer System (JSS) at Japan Aerospace Exploration Agency (JAXA) and High Performance Computing Center (HPCC) at Stanford University. We gratefully acknowledge Professor J. G. Santiago and Professor J. C. Dutton for providing extensive experimental data. We are grateful to our AFOSR-MURI project collaborators, and in particular Professor M. G. Mungal and Dr. W. N. Heltsley for various discussions on the upstream jet fluid mixing, and Dr. V. E. Terrapon for comments on the manuscript. Present code is based on extension to the code FDL3DI provided by Dr. M. R. Visbal, whom we thank for this.

REFERENCES

- BEN-YAKAR, A., MUNGAL, M. G. & HANSON, R. K. 2006 Time evolution and mixing characteristics of hydrogen and ethylene transverse jets in supersonic crossflows. *Phys. Fluids* **18** (2), 026101.
- COOK, A. W. 2007 Artificial fluid properties for large-eddy simulation of compressible turbulent mixing. *Phys. Fluids* **19** (5), 055103.
- EVERETT, D. E., WOODMANSEE, M. A., DUTTON, J. C. & MORRIS, M. J. 1998 Wall pressure measurements for a sonic jet injected transversely into a supersonic crossflow. *J. Propul. Power* **14** (6), 861–868.
- FRIC, T. F. & ROSHKO, A. 1994 Vortical structure in the wake of a transverse jet. *J. Fluid Mech.* **279**, 1–47.
- GAITONDE, D. V. & VISBAL, M. R. 2000 Padé-type higher-order boundary filters for the Navier-Stokes equations. *AIAA J.* **38** (11), 2103–2112.
- GRUBER, M. R., NEJAD, A. S., CHEN, T. H. & DUTTON, C. J. 1995 Mixing and penetration studies of sonic jets in a Mach 2 freestream. *J. Propul. Power* **11** (2), 315–323.
- HELTSLEY, W. N. 2009 Structure and stability of reacting jets in supersonic crossflow. *Ph.D. Thesis in publication* Stanford University.
- IZUKA, N. 2006 Study of Mach number effect on the dynamic stability of a blunt re-entry capsule. *Ph.D. Thesis* The University of Tokyo.
- KAWAI, S. & LELE, S. K. 2008a Large-eddy simulation of jet mixing in a supersonic turbulent crossflow. *Annual Research Briefs*, Center for Turbulence Research, 139–151.
- KAWAI, S. & LELE, S. K. 2008b Localized artificial diffusivity scheme for discontinuity capturing on curvilinear meshes. *J. Comput. Phys.* **227** (22), 9498–9526.
- KAWAI, S., SHANKAR S. K. & LELE, S. K. 2009 Assessment of localized artificial diffusivity scheme for large-eddy simulation of compressible turbulent flows. *J. Comput. Phys.* doi: 10.1016/j.jcp.2009.11.005
- KAWAI, S. & LELE, S. K. 2009 Large-eddy simulation of jet mixing in a supersonic turbulent crossflow. *submitted to AIAA J.*
- LELE, S. K. 1992 Compact finite difference schemes with spectral-like resolution. *J. Comput. Phys.* **103** (1), 16–42.
- MANI, A., LARSSON, J. & MOIN, P. 2009 Suitability of artificial bulk viscosity for large-eddy simulation of turbulent flows with shocks. *J. Comput. Phys.* **228** (19), 7368–7374.
- PETERSON, D. M., SUBBAREDDY, P. K. & CANDLER, G. V. 2006 Assessment of synthetic inflow generation for simulating injection into a supersonic crossflow. *AIAA Paper 2006–8128*.
- SANTIAGO, J. G. & DUTTON, C. J. 1997 Velocity measurements of a jet injected into a supersonic crossflow. *J. Propul. Power* **13** (2), 264–273.
- SHERER, S. E. & VISBAL, M. R. 2003 Computational study of acoustic scattering from multiple bodies using a high-order overset grid approach. *AIAA Paper 2003–3203*.
- SU, L. K. & MUNGAL, M. G. 2004 Simultaneous measurements of scalar and velocity field evolution in turbulent crossflowing jets. *J. Fluid Mech.* **513**, 1–45.
- VANLERBERGHE, W. M., SANTIAGO, J. G., DUTTON, C. J. & LUCHT, R. P. 2000

- Mixing of a sonic transverse jet injected into a supersonic flow. *AIAA J.* **38** (3), 470-479.
- VITI, V., NEEL, R. & SCHETZ, J. A. 2009 Detailed flow physics of the supersonic jet interaction flow field. *Phys. Fluids* **21** (4), 046101.
- VON LAVANTE, E., ZEITZ, D. & KALLENBERG, M. 2001 Numerical simulation of supersonic airflow with transverse hydrogen injection. *J. Propul. Power* **17** (6), 1319-1326.
- URBIN, G. & KNIGHT, D. 2001 Large-eddy simulation of a supersonic boundary layer using an unstructured grid. *AIAA J.* **39** (7), 1288-1295.